

Supporting Information

Rational Design of Covalent Organic Frameworks with High Capacity and Stability as Lithium-ion Battery Cathode

Derong Luo, Jing Zhang, Huizi Zhao, Hai Xu, Xiaoyu Dong, Langyuan Wu, Bing Ding, Hui Dou,* and Xiaogang Zhang*

Jiangsu Key Laboratory of Electrochemical Energy Storage Technologies, College of Materials

Science and Technology, Nanjing University of Aeronautics and Astronautics, Nanjing 210016, P.

R. China.

E-mail: dh_msc@nuaa.edu.cn

E-mail: azhangxg@nuaa.edu.cn

Materials and Characterization

All the chemicals (Nanjing Chemical Reagent Co., Ltd., Aladdin Co., Ltd.) were utilized without further purification. Electrolytes of lithium bis(trifluoromethanesulfonyl)imide (LiTFSI) (1 M in 1,3-dioxolane (DOL)/dimethoxyethane (DME) (1:1 v/v)) and lithium hexafluorophosphate (LiPF₆) (1 M in ethylene carbonate (EC)/diethyl carbonate (DEC) (1:1 v/v)) was brought from Duoduo Reagent.

Fourier transform-infrared spectra were tested on a FT-IR spectrophotometer (Bruker INVENIO-R). Raman spectrum was examined with a Bruker Renishaw inVia using laser excitation at 514.5 nm. Nuclear magnetic resonance (NMR) spectra were recorded on a 400M Bruker AVANCE III HD 400. ¹³C cross-polarization with magic angle-spinning (CP-MAS) solid-state nuclear magnetic resonance spectra were recorded on a Bruker ARX 300 MHz spectrometer. Powder X-ray patterns (PXRD) were collected on a Bruker-AXS D8 DISCOVER instrument with a diffractometer using Cu K α radiation and the scan rate was 5° min⁻¹ from 2° to 40°. Thermal gravimetric analyses (TGA) were performed on a Perkin-Elmer TGA 7 under N₂ atmosphere with a heating rate of 5° min⁻¹. X-ray photoelectron spectroscopy (XPS) was carried out with a Perkin-Elmer PHI 550 with Al-K α as the X-ray source. Electron energy dispersive spectroscopy (EDS), scanning electron microscopy (SEM) and high resolution transmission electron microscope (HRTEM) were characterized on the JEOL JSM-6380LV and JEOL JEM-2010, respectively.

Electrochemical measurements

Electrical conductivity measurement was carried out by preparing the NTCDI-COF plates under a pressure of 25 MPa at room temperature and sputtering gold on both sides of the plates for 200 s. The diameter and thickness of the plates is 13 mm and 0.33 mm, respectively. The plates were sandwiched by two stainless steel chips connected to electrochemical workstation (Biologic VMP-300). The change of the transient current at 4.2 V was tested until the current stabilizes, from which the resistivity and conductivity of NTCDI-COF cathode were calculated. The CR-2032 type coins were assembled in an argon-filled glove box with both moisture and oxygen contents below 0.01ppm, and pure lithium foils were used as the counter electrodes. The mixture of NTCDI-COF powder (active material), acetylene black (conducting agent), and polyvinylidene difluoride (PVDF, binder) with a mass ratio of 6:3:1 dispersed in N-methylpyrrolidone (NMP) solution was loaded onto the aluminium foil and then dried at 110° for 12 h under vacuum to produce the working electrode. The areal loading of the active material on the current collector was 0.6~0.8 mg cm⁻². Graphite paste was loaded onto the copper foil (Graphite:acetylene black:PVDF in a mass ratio of 8:1:1). 1 M LiTFSI and 1 M LiPF₆ was served as the electrolytes. The cyclic voltammetry (CV, voltage range: NTCDI-COF half-cell of 1.5-3.5 V, full cell of 0.05-2.6 V) and electrochemical impedance spectroscopy (EIS, frequency range: 10⁵-0.01 Hz, scan rate of 5 mV s⁻¹) tests were carried on the electrochemical workstation (Biologic VMP-300). The NTCDI-COF cathode and graphite anode were assembled into 2016-type coin cell before assembling the full

cells, respectively, and were prelithiated by electrochemical prelithiation method at a current density of 0.1 A g⁻¹ for 3 cycles. The electrodes disassembled from the half cells were further used to assemble the full cells of NTCDI-COF//graphite in 2032-type coin, the specific capacity for the full cells was based on the NTCDI-COF cathode. Long cycling galvanostatic charge-discharge tests were performed on the LAND test system. All the electrochemical tests were performed at room temperature.

DFT calculations

The geometry of all molecules was optimized through density functional theory (DFT). All the DFT computations were performed by the B3LYP density functional method with the GD3BJ dispersion correction.^{1, 2} And 6-31+G** basis set was employed. All these calculations were performed with Gaussian 16 software package.

Theoretical capacity calculation of NTCDI-COF

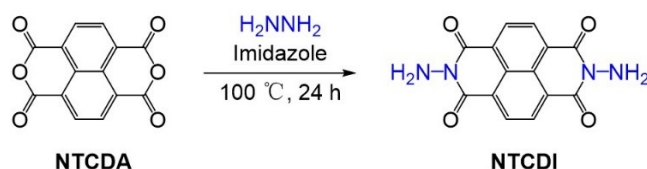
Theoretical capacity C_t (mA h g⁻¹) was calculated using the following equation³:

$$C_t = \frac{nF}{3600(M_w/1000)}$$

Where n is the number of electrons transferred per redox reaction, F is the Faraday constant (96485 C mol⁻¹), and M_w is the molar weight of the repeat unit of NTCDI-COF (316 g mol⁻¹)

Experimental section

Synthesis of 2,7-diaminobenzo[*lmn*][3,8]phenanthroline-1,3,6,8(2H,7H)-tetraone (NTCDI):



NTCDI was synthesized according to reported method ⁴. 1,4,5,8-Naphthalenetetracarboxylic dianhydride (NTCDA, 2.7 g, 10 mmol) was dissolved in imidazole (25 g). Then, hydrazine hydrate (2.5 g, 5 mmol) was added into above solution after complete melting of imidazole by heating, stirred at $100\text{ }^\circ\text{C}$ for 17 h. After cooled to temperature, 1 L of 2 M HCl was added into the system. The precipitate was collected by filtration and washed sequentially with 2 M HCl and distilled water. The yellow NTCDA powder was obtained after dried in vacuum at $110\text{ }^\circ\text{C}$ for 12 h with a yield of 90 %. ^1H NMR (400 MHz, $\text{DMSO-}d_6$) δ 8.57 (d, $J = 7.5$ Hz, 4H), 5.85 (s, 4H). ^{13}C NMR (101 MHz, $\text{DMSO-}d_6$) δ 168.86, 137.18, 130.56, 129.75. FT-IR (KBr): 3324, 3247, 1719, 1704, 1659, 1560, 1388, 1282, 1241 and 948 cm^{-1} .

Synthesis of NTCDI-COF

NTCDI (89 mg, 0.3 mmol), hexaketocyclohexane octahydrate (HKH, 17 mg, 0.1 mmol), N,N-dimethylformamide (DMF, 2 mL), 1,2-dichlorobenzene (*o*-DCB, 2 mL) and 6 M HAc (0.2 mL) were added to a 15 mL Pyrex tube. After sonication for 10 min, the Pyrex tube was treated for three freeze-pump-thaw cycles, and then flame sealed. After cooling to room temperature, the sealing Pyrex tube was kept in an oven

at 120 °C for 3 days. The precipitate was collected by filtration and washed with DMF and acetone, then purified by Soxhlet extraction for 24 h with tetrahydrofuran (THF) as solvent. The powder was collected and dried in vacuum at 80 °C for 12 h to afford dark-brown NTCDI-COF powder with a 75% yield. FT-IR (powder, KBr): 1706, 1618, 1581, 1442, 1318, 1242, 1198, 979 and 877 cm^{-1} .

The synthesis of NTCDI-COF was performed in different solvent composition of N,N-dimethylacetamide (DMAc)/1,4-dioxane, DMAc/*o*-DCB, DMAc/mesitylene, mesitylene/1,4-dioxane, 1-butanol (*n*-BuOH)/mesitylene, *n*-BuOH/ *o*-DCB, DMF/1,4-dioxane (in a volume ratio of 2 mL/2 mL) to determine the effect of solvent on the crystallinity of the product (Fig. S4 and S5).

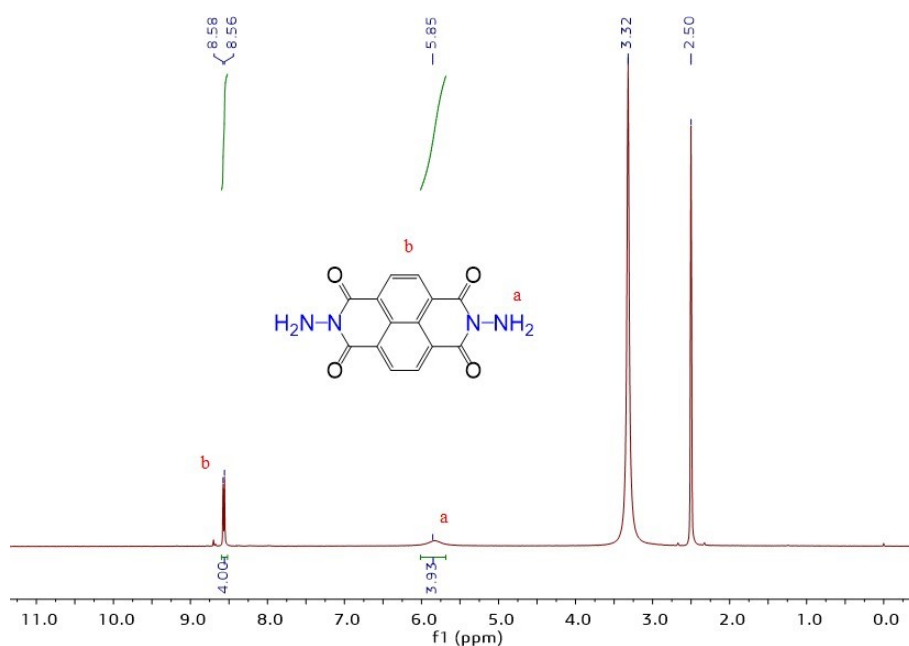


Fig. S1 The ^1H NMR (400 MHz, $\text{DMSO}-d_6$) spectrum of NTCDI.

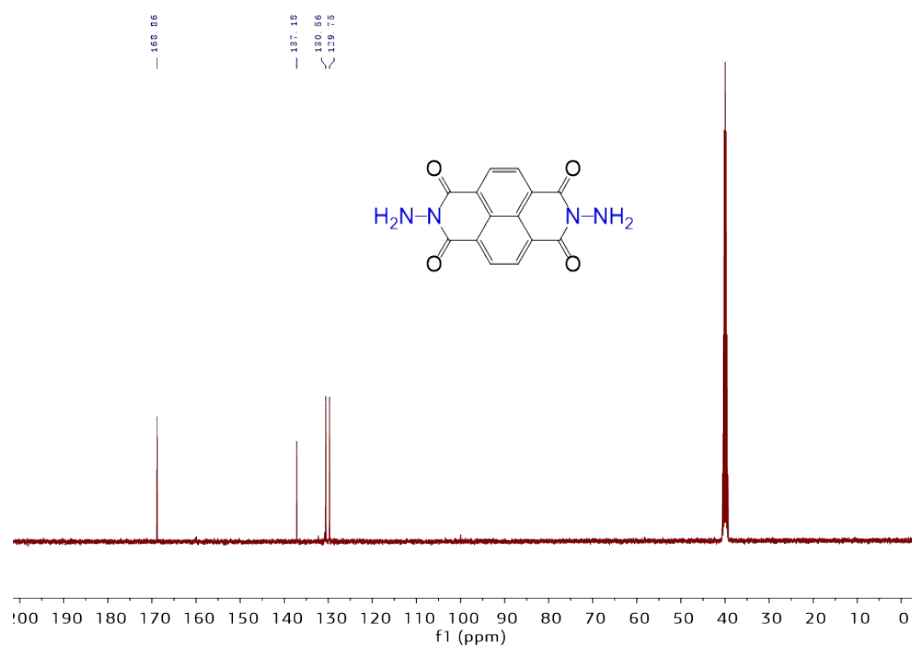


Fig. S2 The ^{13}C NMR (101 MHz, $\text{DMSO-}d_6$) spectrum of NTCDI.

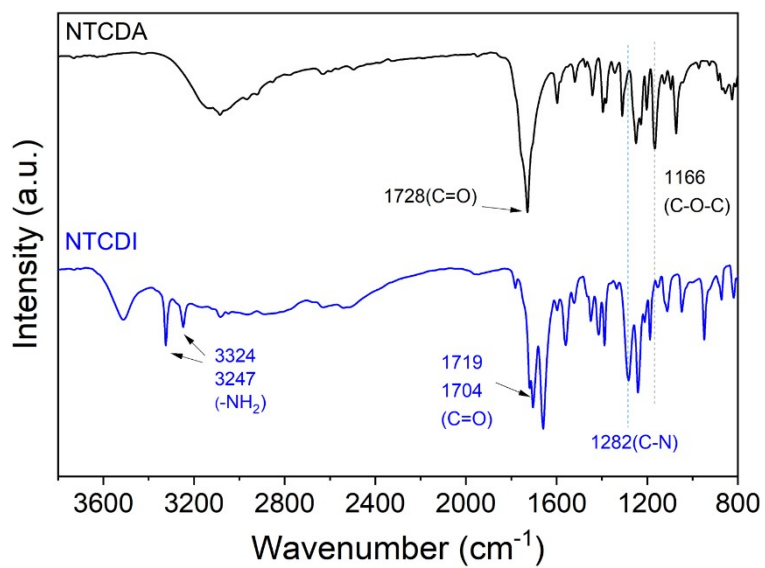


Fig. S3 The FT-IR spectra of NTCDI and NTCDI.

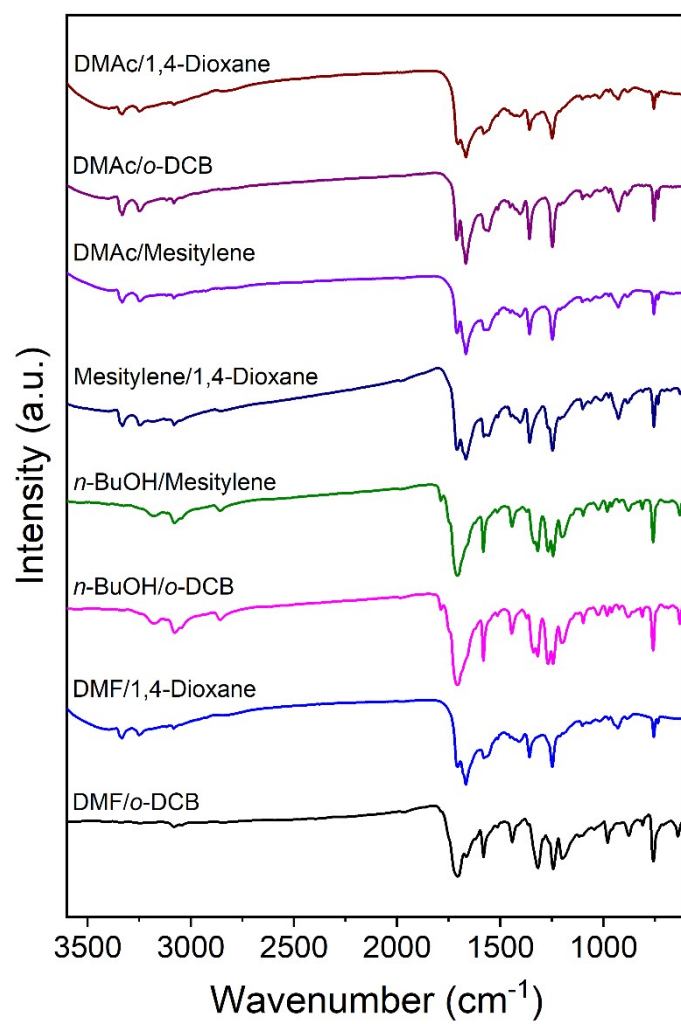


Fig. S4 The FT-IR spectra of NTCDI-COF synthesized with different solvents.

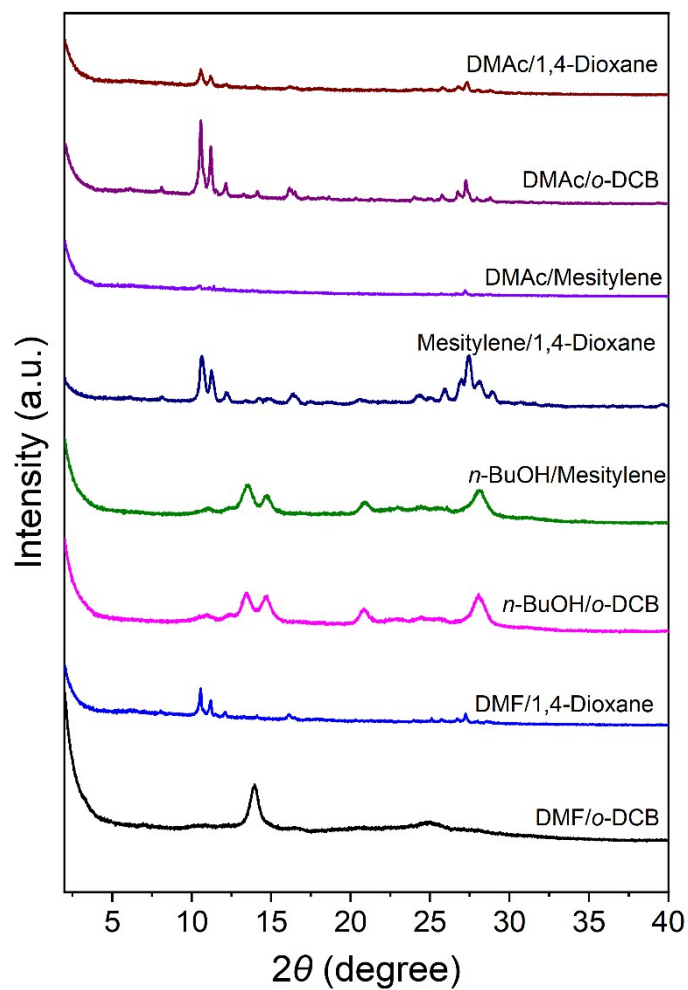


Fig. S5 The PXRD patterns of NTCDI-COF synthesized with different solvents.

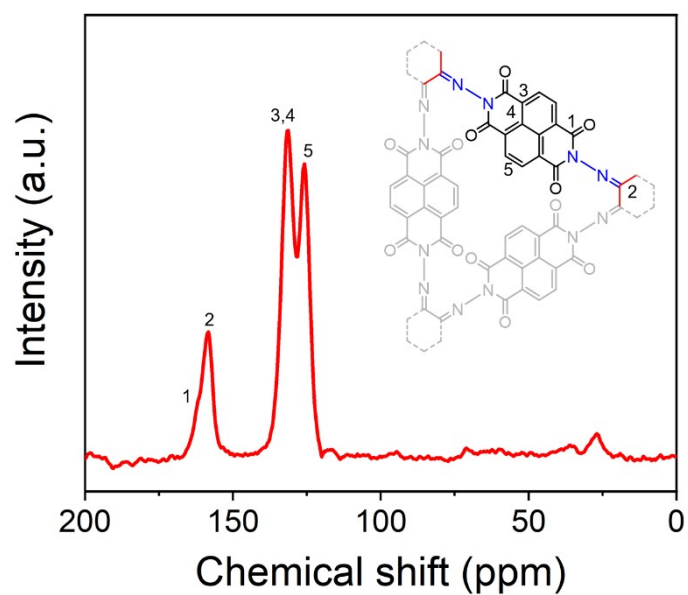


Fig. S6 The solid state ^{13}C NMR spectrum of NTCDI-COF.

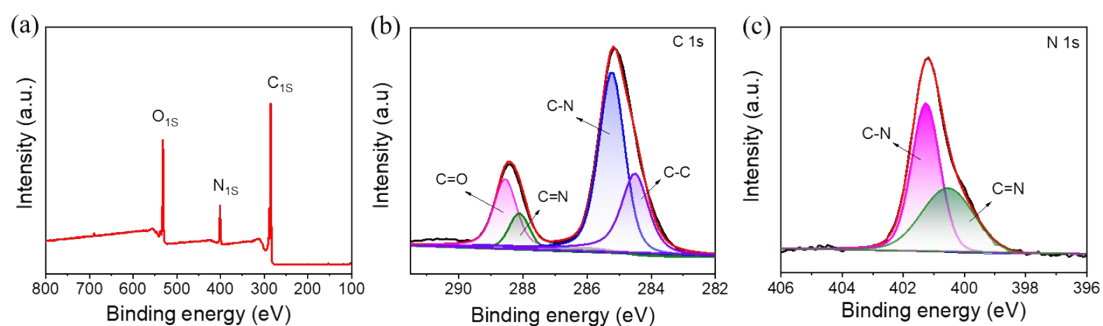


Fig. S7 XPS spectrum of NTCDI-COF. (a) Full survey, (b) C1s XPS spectrum, (c) N1s XPS spectrum.

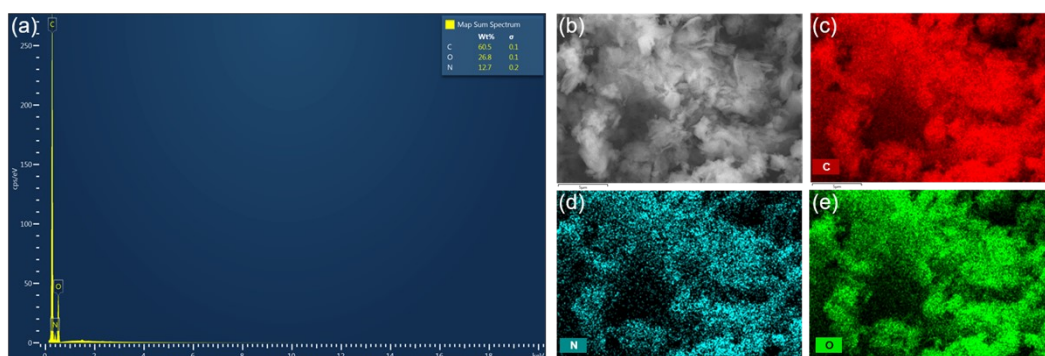


Fig. S8 EDS spectrum of NTCDI-COF. (a) The elemental composition (C, N and O), (b) SEM images, (c-e) Corresponding element distributions for C, N and O.

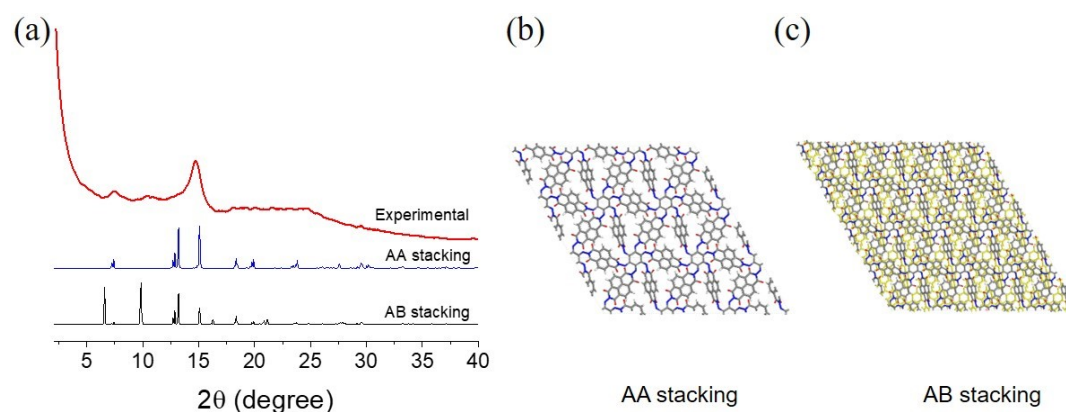


Fig. S9 (a) PXRD patterns of NTCDI-COF, (b) The structure of NTCDI-COF in AA stacking mode, (c) The structure of NTCDI-COF in AB stacking mode (color of elements: C, gray; H, white; N, blue; O, red). (P1, $a=13.77 \text{ \AA}$, $b=13.94 \text{ \AA}$, $c=6.70 \text{ \AA}$, $\alpha=\beta=90^\circ$, $\gamma=120^\circ$)

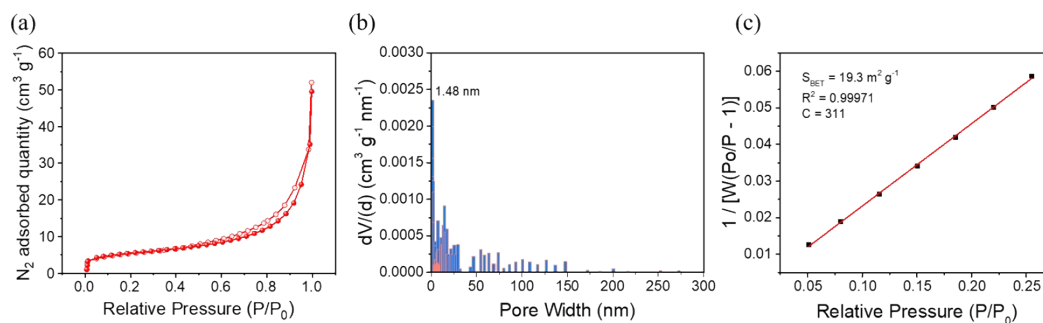


Fig. S10 Nitrogen sorption experiment (77 K) of NTDCI-COF. (a) Nitrogen sorption isotherm, (b) Pore size distribution, (c) Multi-point BET surface area.

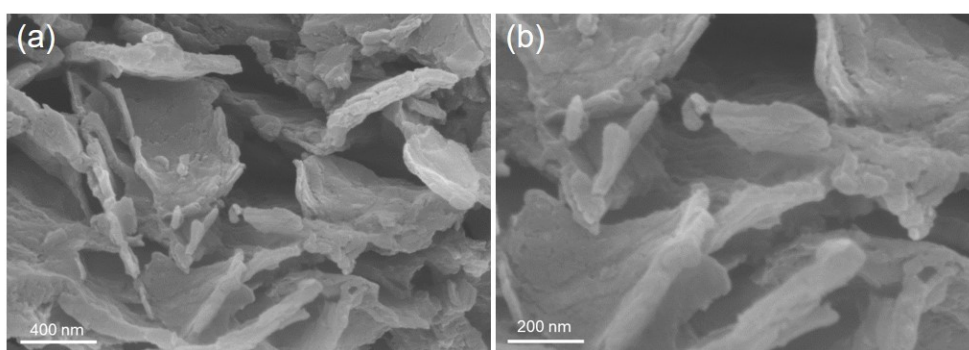


Fig. S11 SEM images of NTDCI-COF.

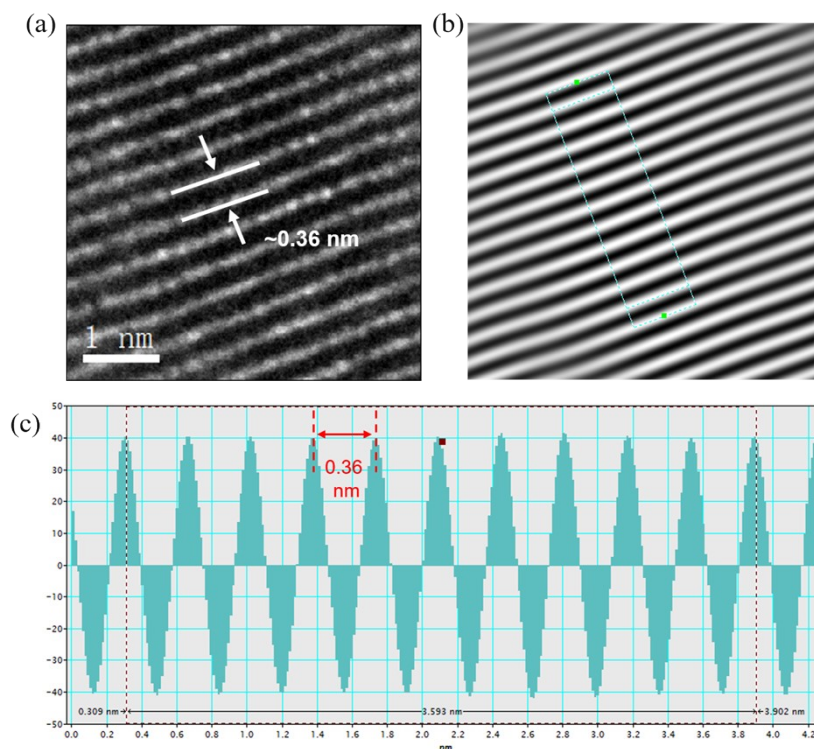


Fig. S12 Lattice fringe distance measurement of NTDCI-COF.

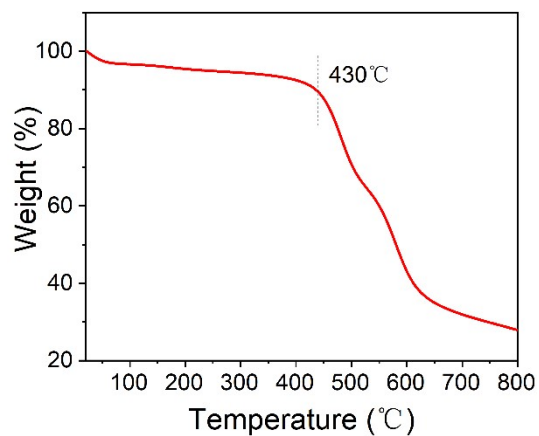


Fig. S13 TGA curve of NTCDI-COF under a N_2 atmosphere.

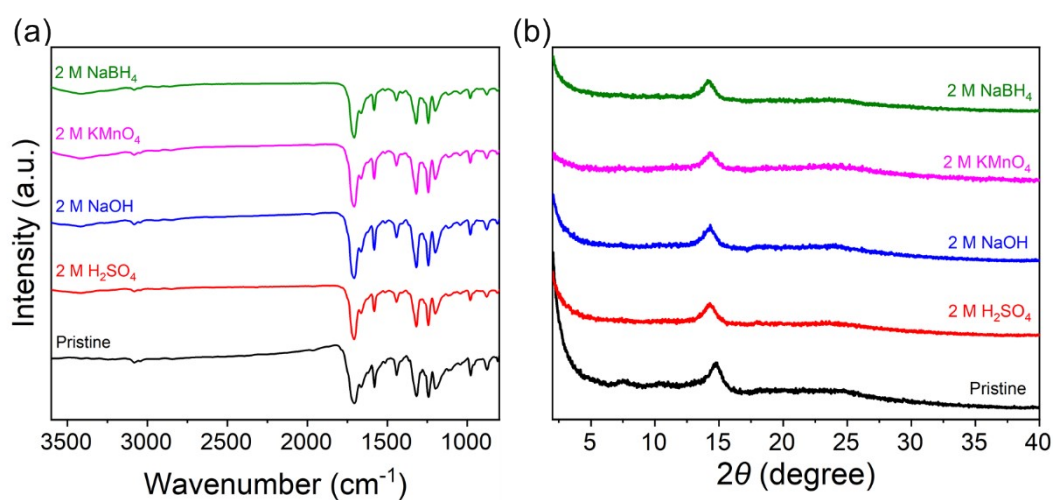


Fig. S14 Chemical stability of NTCDI-COF after respectively immersed in 2 M $NaBH_4$, 2 M $KMnO_4$, 2 M $NaOH$, and 2 M H_2SO_4 at ambient temperature for 3 days.

(a) FT-IR spectra, (b) PXRD patterns.

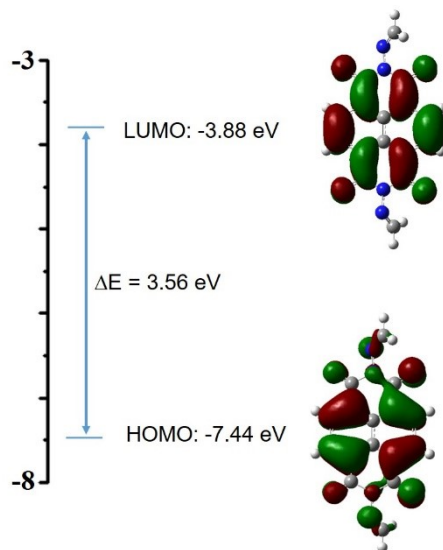


Fig. S15 Optimized molecular structures and HOMO/LUMO energy levels of the repeating unit of NTCDI-COF.

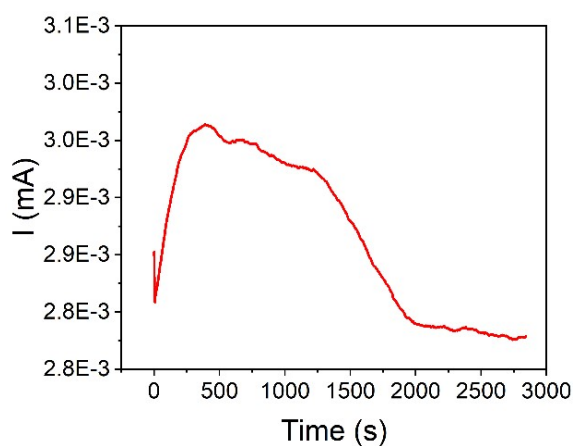


Fig. S16 *I-t* curve of NTCDI-COF.

The electrical conductivity is calculated using the following formula³.

$$\sigma = \frac{1}{\rho}$$

$$\rho = \frac{V}{I} \times \frac{S}{L}$$

The conductivity σ (S m^{-1}) was calculated as $\sigma = \frac{I}{V} \times \frac{L}{S}$.

$\frac{I}{V}$ is the ratio of steady current to voltage, the L and S is the thickness and area of NTCDI-COF flakes, respectively. The ρ represents the resistivity.

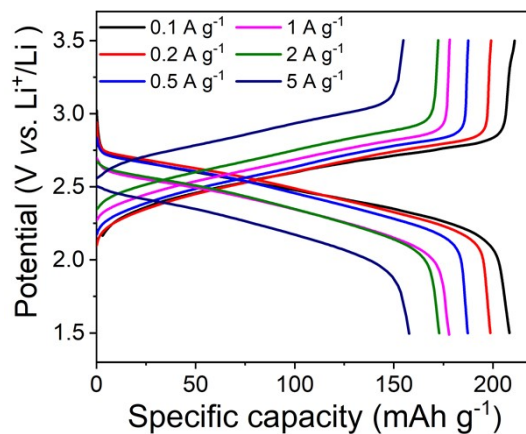


Figure S17 The second discharge/charge curves at various current rates from 0.1 to 5 A g^{-1} .

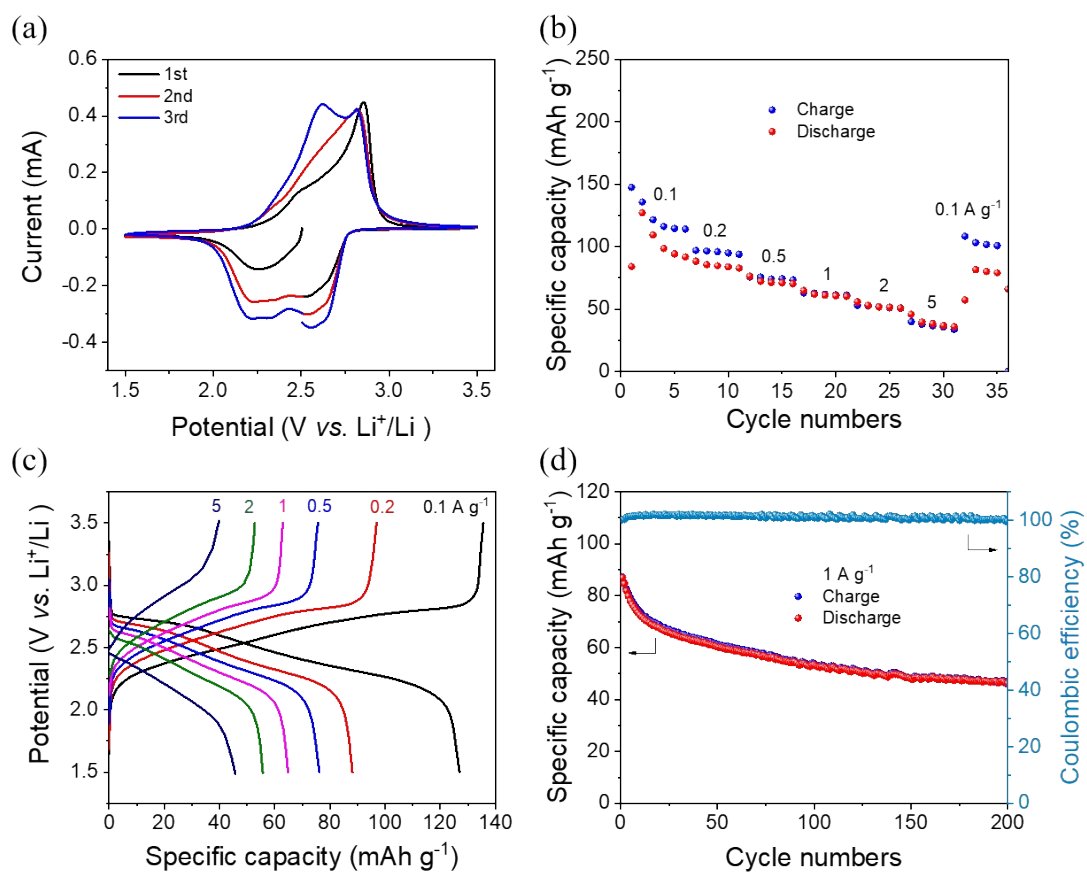


Fig. S18 The electrochemical performance of NTCDI-COF with 1 M LiPF_6 (EC/DMC, 1:1 v/v) as electrolyte. (a) CV curves at 1 mV s^{-1} . (b) Rate performance at

current densities from 0.1 to 5 A g⁻¹. (c) The second discharge/charge curves at current densities from 0.1 to 5 A g⁻¹. (d) Cycling stability at 1 A g⁻¹.

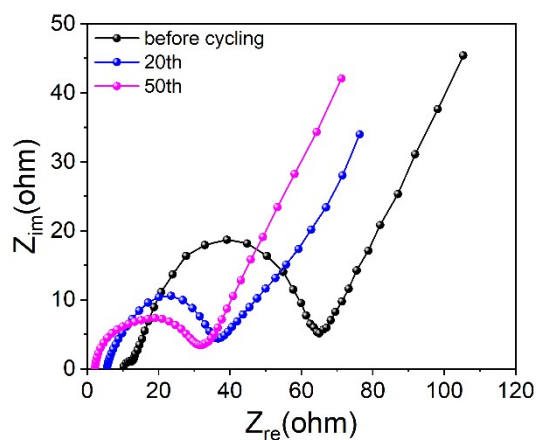


Fig. S19 Nyquist plots of NTCDI-COF before and after different cycles at 1 A g⁻¹.

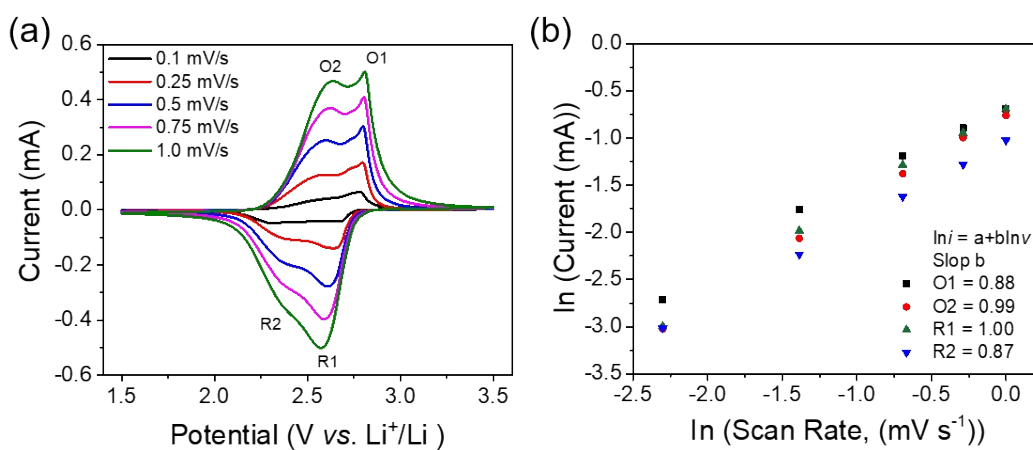


Fig. S20 (a) CV curves of NTCDI-COF at different sweep rates, (b) $\ln i$ versus $\ln v$ plots to determine the b values of different peaks.

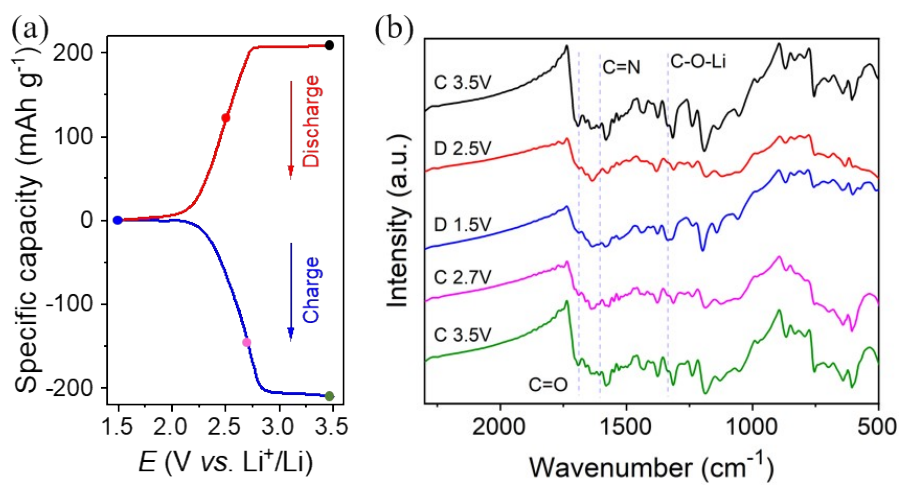


Fig. S21 (a) The second discharging/charging profiles of NTCDI-COF at 0.1 A g^{-1} , (b) The *ex situ* FT-IR spectra of NTCDI-COF in the corresponding discharged/charged states.

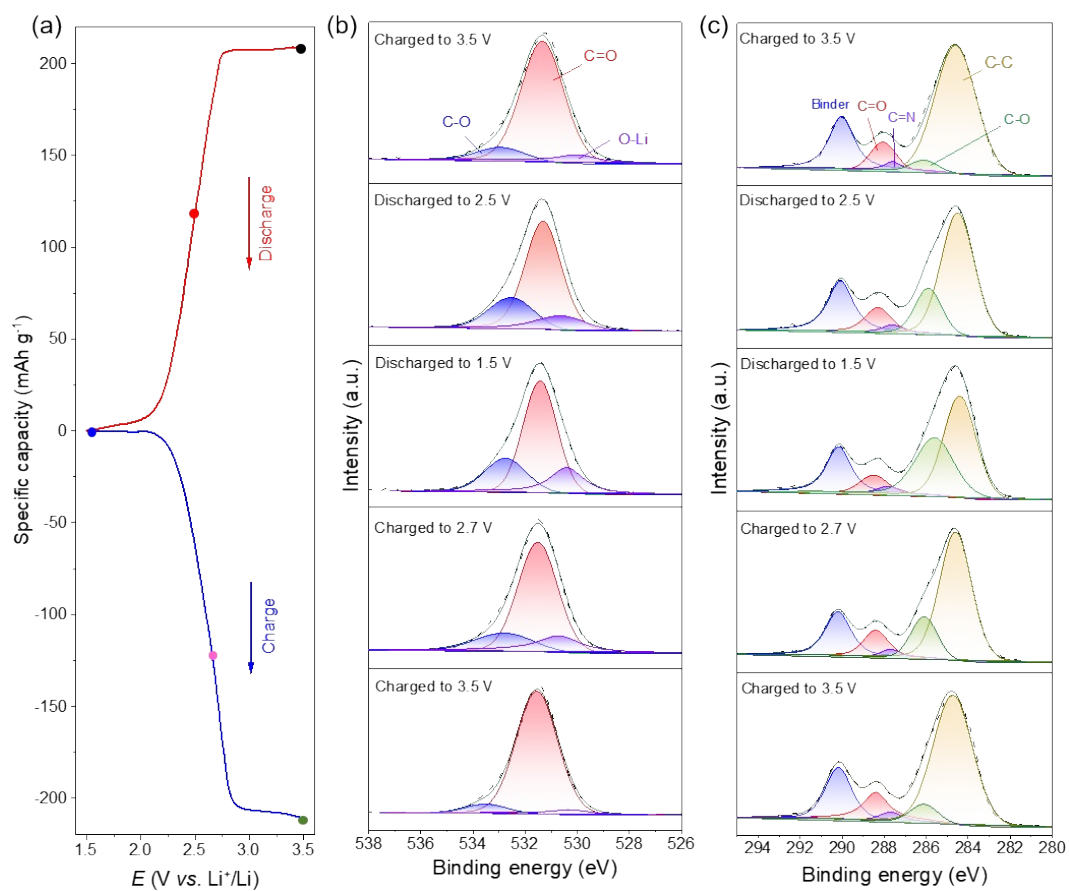


Fig. S22 (a) The second discharging/charging profiles of NTCDI-COF at a current density of 0.1 A g⁻¹. High-resolution *ex situ* XPS spectra of O 1s (b) and C 1s (c) in the corresponding discharged/charged states.

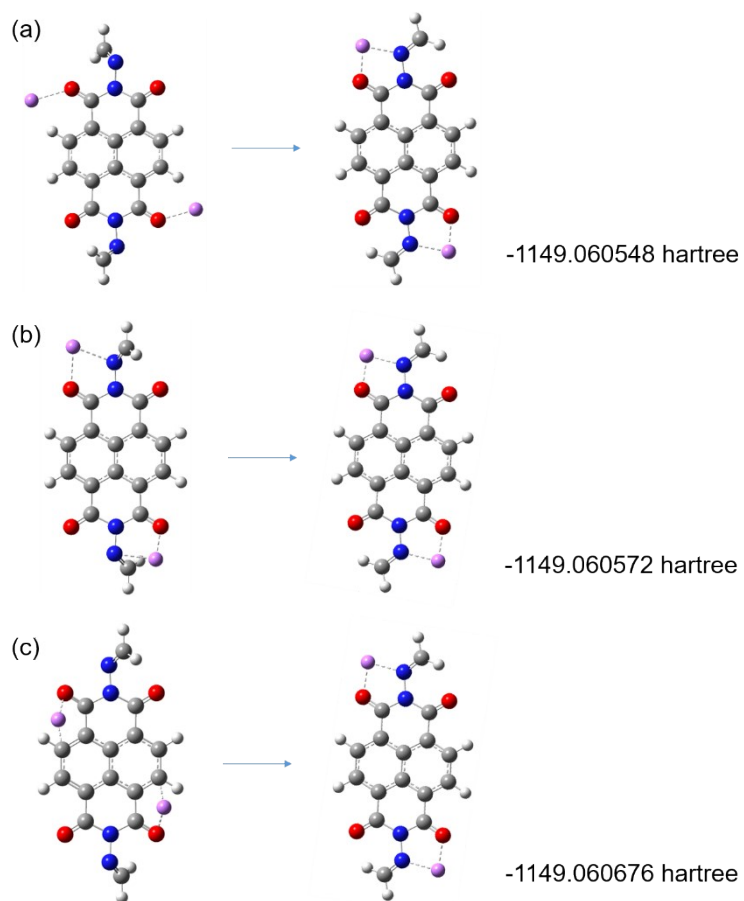


Fig. S23 Possible configurations and optimized structure of NTCDI-COF-2Li. (color of elements: C, gray; H, white; N, blue; O, red; Li⁺, purple).

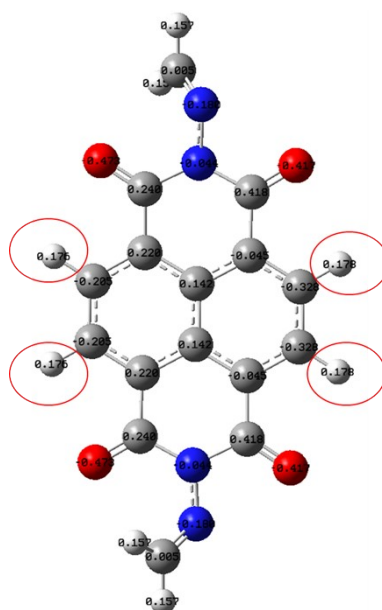


Fig. S24 Mulliken charge distribution of NTCDI-COF repeating unit. (color of elements: C, gray; H, white; N, blue; O, red).

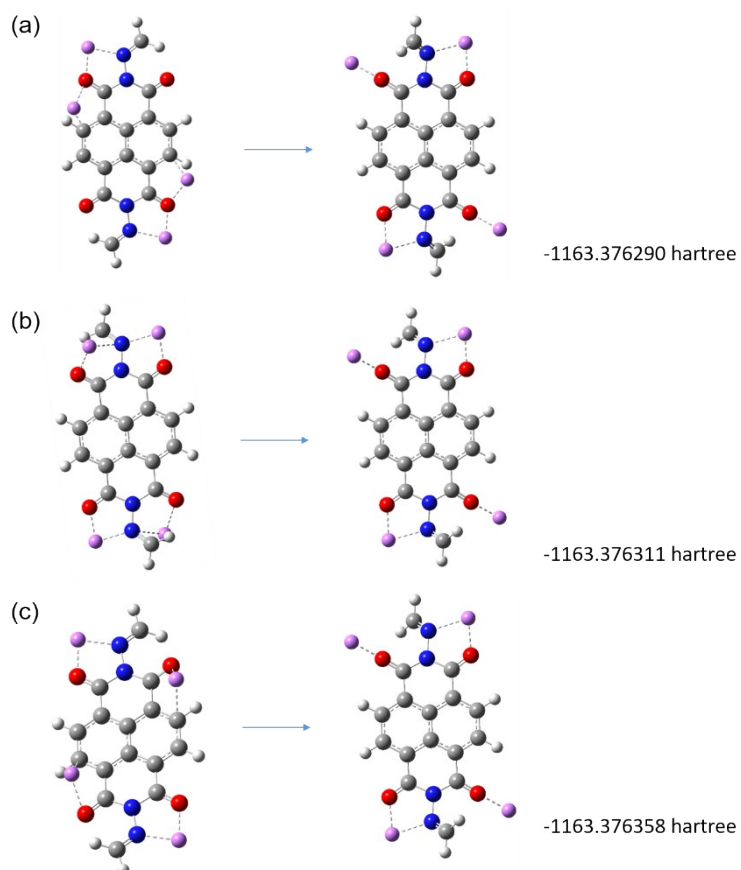


Fig. S25 Possible configurations and optimized structure of NTCDI-COF-4Li. (color of elements: C, gray; H, white; N, blue; O, red; Li^+ , purple).

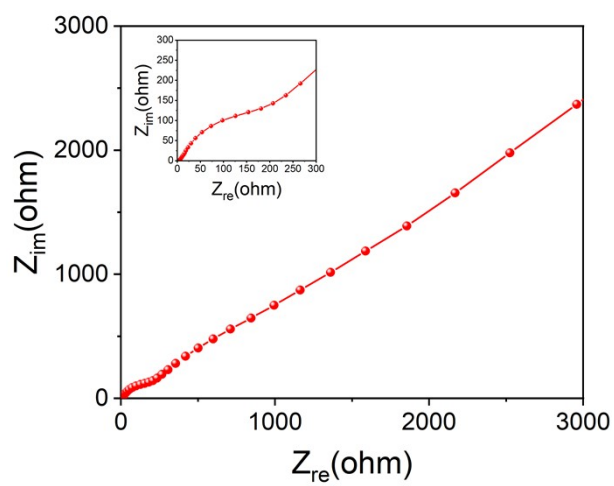


Fig. S26 EIS of NTCDI-COF//graphite full cells at 5 mV s⁻¹.

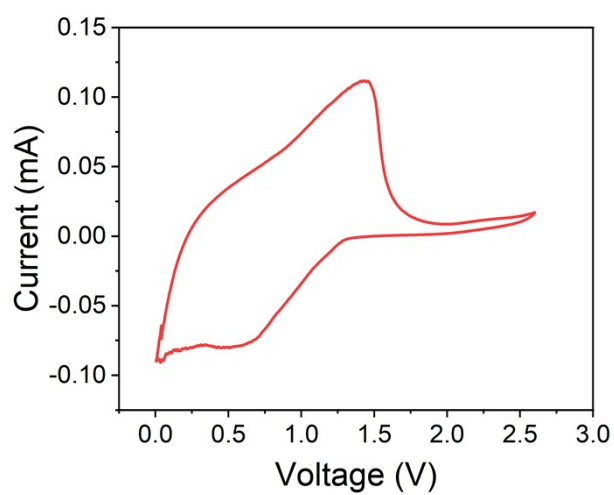


Fig. S27 CV curve of NTCDI-COF//graphite full cells at 0.5 mV s⁻¹.

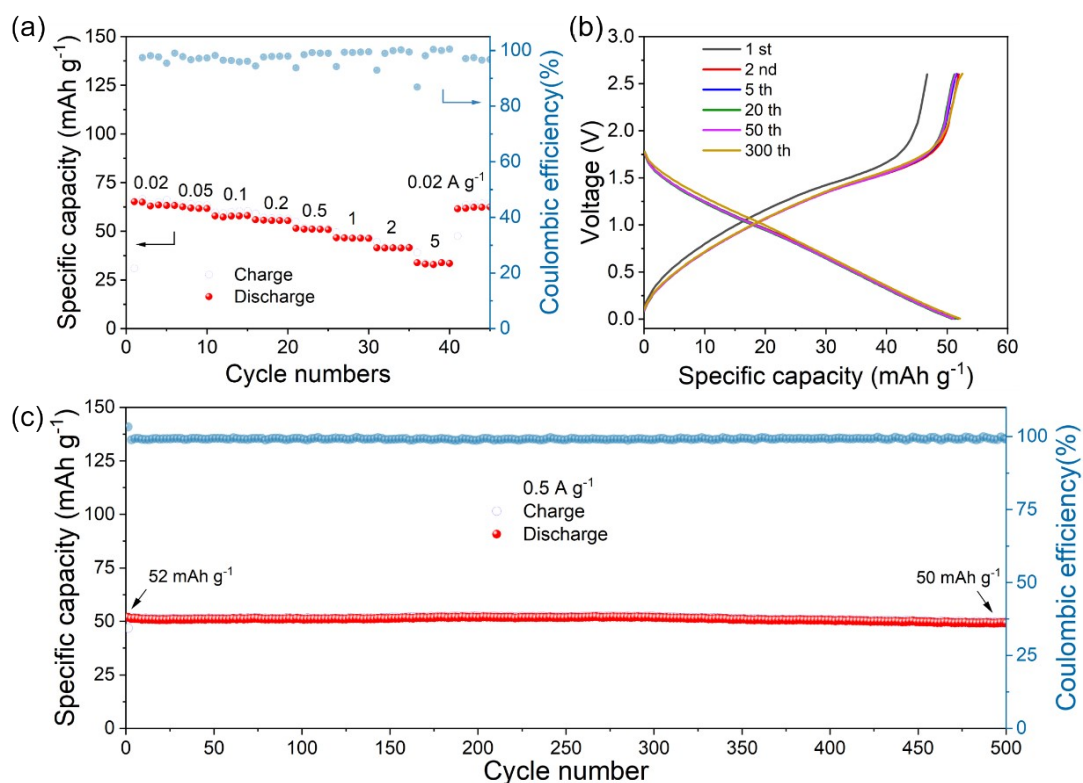
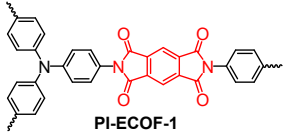
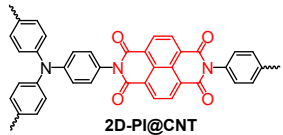


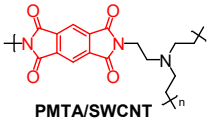
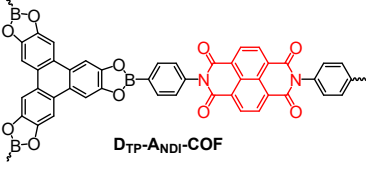
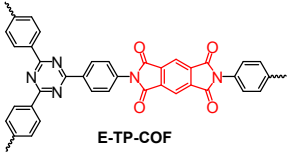
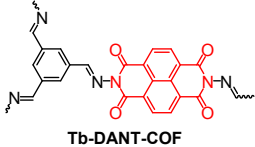
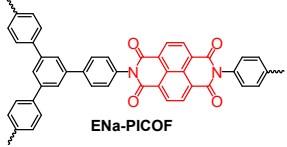
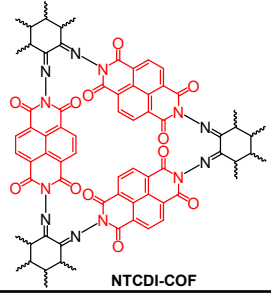
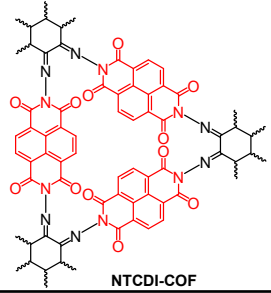
Fig. S28 Electrochemical performance of NTCDI-COF//graphite full cells. (a) Rate performance. (b) The charge/discharge curves of different cycles at 0.5 A g⁻¹. (c) Long-term cycling stability at 0.5 A g⁻¹.

Considering the outstanding performance of NTCDI-COF cathode in half-cells, constructed the Li-ion full cells with the NTCDI-COF and commercial graphite. Notably, before matching the full cells, the Li⁺ were intercalated into NTCDI-COF cathode and graphite anode to form solid electrolyte interphase (SEI) by electrochemical prelithiation method. Therefore, the reduction state of NTCDI-COF and oxidation state of graphite was employed as the starting cathode and anode of full cells, respectively. The EIS of the full cell shows fast charge transfer capability (Fig. S26). Delightfully, the full cells of NTCDI-COF//graphite deliver a discharge capacity of 65 mAh g⁻¹ in 0.05-2.6 V at a current density of 0.02 A g⁻¹ (Fig. S27 and S28a),

corresponding to an energy density of 48 Wh kg⁻¹. Meanwhile, the full cells realize a good rate performance of 65/63/58/56/52/47/42/34 mAh g⁻¹ at current densities of 0.02/0.05/0.1/0.2/0.5/1/2/5 A g⁻¹ (Fig. S28a) respectively, and recovers rapidly to 62 mAh g⁻¹ when the current density is abruptly switched from 5 A g⁻¹ to 0.02 A g⁻¹. Finally, the long-term cycle performance of full cells at 0.5 A g⁻¹ was tested. The NTCDI-COF//graphite full cells show remarkable cycling stability (Fig. S28b) with a specific capacity of 50 mAh g⁻¹ and an energy density of 40 Wh kg⁻¹ after 500 cycles (more than 99% coulombic efficiency and over 96% capacity retention) (Fig. S28c).

Table. S1 The electrochemical performance comparison of NTCDI-COF cathode with other COFs cathode.

Cathode materials	Current densities (mA g ⁻¹)	Capacities (mAh g ⁻¹)	Capacity retentions	Refs
 PI-ECOF-1	142	152 (add rGO)	69% after 300 cycles	5
 2D-PI@CNT	100	104.4 (add CNT)	~100% after 50 cycles	6

	192	147 (add SWCNT)	86.6% after 200 cycles	7
	200	42	48% after 50 cycles	8
	200	110	87% after 500 cycles	9
	200	123.7	67% after 200 cycles	10
	50	95	92% after 100 cycles	11
	100	210	82% after 100 cycles	This work
	2000	146	86% after 1500 cycles	This work

References

1. S. Grimme, J. Antony, S. Ehrlich and H. Krieg, *J. Chem. Phys.*, 2010, **132**, 154104.
2. S. Grimme, S. Ehrlich and L. Goerigk, *J. Comput. Chem.*, 2011, **32**, 1456–1465.
3. M. Wu, Y. Zhao, B. Sun, Z. Sun, C. Li, Y. Han, L. Xu, Z. Ge, Y. Ren, M. Zhang, Q. Zhang, Y. Lu, W. Wang, Y. Ma and Y. Chen, *Nano Energy*, 2020, **70**, 104498.
4. H. Langhals and A. Hofer, *J. Org. Chem.*, 2013, **78**, 5889–5897.
5. Z. Wang, Y. Li, P. Liu, Q. Qi, F. Zhang, G. Lu, X. Zhao and X. Huang, *Nanoscale*, 2019, **11**, 5330–5335.
6. G. Wang, N. Chandrasekhar, B. P. Biswal, D. Becker, S. Paasch, E. Brunner, M. Addicoat, M. Yu, R. Berger and X. Feng, *Adv. Mater.*, 2019, **31**, 1901478.
7. H. Wu, Q. Meng, Q. Yang, M. Zhang, K. Lu and Z. Wei, *Adv. Mater.*, 2015, **27**, 6504.
8. F. Xu, S. Jin, H. Zhong, D. Wu, X. Yang, X. Chen, H. Wei, R. Fu and D. Jiang, *Scientific Reports*, 2015, **5**, 1–6.

9. G. F. Zhao, H. Li, Z. H. Gao, L. Xu, Z. Y. Mei, S. Cai, T. T. Liu, X. F. Yang, H. Guo and X. L. Sun, *Adv. Funct. Mater.*, 2021, **31**, 2101019–2101028.
10. D. Yang, Z. Yao, D. Wu, Y. Zhang, Z. Zhou and X. Bu, *J. Mater. Chem. A*, 2016, **4**, 18621–18627.
11. S. Gu, X. Ma, J. Chen, R. Hao, Z. Wang, N. Qin, W. Zheng, Q. Gan, W. Luo, M. Li, Z. Li, K. Liao, H. Guo, G. Liu, K. Zhang and Z. Lu, *Journal of Energy Chemistry*, 2022, **69**, 428-433.